10
Transport Phenomena in Microscale Reacting Flows

Niket S. Kaisare, Georgios D. Stefanidis, and Dionisios G. Vlachos

10.1
Introduction

Transport phenomena are crucial in the scale-up of conventional, large-scale chemical reactors because many processes are heat and/or mass transfer controlled. Since transport coefficients are typically inversely proportional to the characteristic dimension of the system, miniaturization of chemical systems leads to a substantial increase in transport rates. This increase in turn enhances the overall rate of processes that are transport limited, leading to considerable process intensification, i.e. the same throughput can be achieved with a much smaller device and thus with much lower capital. Alternatively, much higher throughput can be achieved using a system of the same size as a conventional one, but made up of many small components (scaling out).

Aside from process intensification, the enhanced transport rates may render a microscale system gradientless. This fact has important ramifications for operation and fundamental studies. Examples include elimination of detrimental hot spots caused by very exothermic reactions and the possibility of a microchemical system being isothermal and kinetically controlled. The latter makes microchemical systems ideal for extraction of intrinsic chemical kinetics.

Short diffusion time scales, due to shrinking the device's characteristic dimension, have some other important implications regarding the stability of gas-phase radical chemistry and process safety [1]. Specifically, gas-phase radicals diffuse rapidly to walls where they may recombine to produce stable molecules. As a result, radical-driven chemistries, such as gas-phase combustion, become susceptible to extinction [1]. This radical quenching is a major stumbling block in stabilizing radical-driven homogeneous chemistry (e.g. flames) in confined spaces and thus our ability to scale down processes that rely on heat supply of combustibles. One such example is the traditional steam reforming coupled with combustion of natural gas for syngas production, the scale down of which is particularly difficult [2–4]. At the same time,

Micro Process Engineering, Vol.1: Fundamentals, Operations and Catalysts
Edited by V. Hessel, A. Renken, J.C. Schouten, and J.-I. Yoshida

ISBN: 978-3-527-31550-5

recombination of radicals at walls creates safer devices with respect to accidents and is behind the success of flame arresters.

Due to the small characteristic dimension, the flow in microchemical systems is laminar. As a result, mixing relies only on molecular diffusion instead of the more efficient turbulence that large-scale systems typically exhibit. At the same time, the diffusion time scale is much shorter due to the small size of a microscale device. However, structural elements that play the role of static micromixers may be necessary to spread fast flows, enhance fluid–solid contact, increase mixing of incoming gases, etc. One such example is the post-micromixer discussed in Ref. [5].

From the prolegomena, some questions naturally arise. For example, should one ever worry about gradients in microchemical systems? At normal operating conditions (e.g. 1 atm), the mean free path of gases is a fraction of 1 μm and, given typical reactor sizes, the continuum approximation is still valid. With this in mind, are transport correlations developed for large-scale counterparts applicable to microscale devices? Quenching of gas-phase radicals on walls is obviously much more important for small devices, but are there any other phenomena which are unimportant for large-scale systems that one should account for in modeling microchemical systems?

This chapter focuses on transport phenomena in microreactors whose characteristic dimension [e.g. diameter or gap size (distance between two parallel plates) for wide rectangular-shaped channels] is in the micron scale regime (<1 mm). Specific systems examined include gas-phase (homogeneous) microreactors and gas–solid (heterogeneous) microreactors. Comparison of the two classes reveals key similarities and differences. The chemistries chosen here are some of the faster and most exothermic ones (e.g. homogeneous or catalytic combustion of propane, hydrogen and methane). This judicious choice of chemistries pushes the limits of operation and provides valuable insights into the aforementioned questions. At the same time, these processes are an integral part of the thermochemical conversion of fossil fuels and biomass to hydrogen and chemicals and constitute the foundation for portable electronics and distributed energy production. Since phenomena for these reacting flows are strongly coupled (e.g. temperature profiles affect rates of chemical reactions and these in turn mass transfer), this chapter addresses multiple facets of transport phenomena in these microchemical devices.

The organization of this chapter is as follows. First, the existence of spatial gradients is discussed, then the effect of radiation is addressed. Transverse transport correlations are elucidated and subsequently applications from gas-phase microburners and catalytic microreactors are presented. Finally, conclusions are drawn.

10.2
Spatial Gradients in Microchannels

The term microchemical describes downsizing of a system such that its critical dimension is less than 1 mm. For tubular microreactors, this size reduction entails the tube radius, R, whereas for microchannels of a rectangular entrance section, this entails the height (also referred to as gap size), d, and possibly its width, w. The latter

structures are typically easier to integrate (by stacking them on top of each other) into multifunctional devices than cylindrical structures. Due mainly to conversion constraints, a long longitudinal dimension, L ($L \gg d$ or R) is required to provide sufficient residence time for high conversion.

Gradients depend on the ratio of time scales of various transport and chemical processes. Diffusion (conduction) time scales can easily be estimated from the square of the corresponding length scale divided by the diffusivity (thermal diffusivity). Temperature usually has a fairly small effect on transport time scales (an exception is surface diffusion that is often activated). On the other hand, the time scale of reaction depends very strongly on the chemistry (process) itself and the temperature (via Arrhenius kinetics) and secondary on species concentrations and pressure. Discontinuity at the walls (e.g. slip, lack of thermal accommodation) may also be encountered, but since these phenomena depend on transverse gradients, which are smaller than in large devices, are by-and-large less important in microdevices [1].

10.2.1
Axial Thermal Gradients

Figure 10.1 shows the typical time scale estimates of various transport processes in a microreactor. Since the reactor length is fairly large, the longitudinal time scales of heat conduction in the gas phase and species diffusion are large. One can control the longitudinal time scale of convective flow and thus the longitudinal Peclet number (Pe), by varying the inlet velocity. For reacting systems with a residence time in the millisecond range (high axial Peclet numbers), axial gas-phase diffusion and conduction are negligible ($Pe \gg 1$) in comparison with convection (convection-dominated processes). Since conduction along the wall is much faster than in the gas phase, the former mechanism is dominant in microchemical systems (see also below). As a result, the time scale for longitudinal heat transfer along the wall, which is usually larger than the heat release (or consumption) time scale, mainly controls the axial temperature profiles. Of course, coupling of the wall with the fluid phase via transverse heat transfer is also important, but the transverse transport mechanism is typically much faster (Figure 10.1).

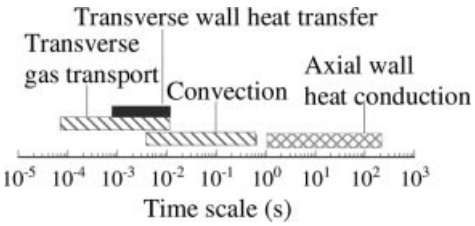

Figure 10.1 Typical transport time scales in microchemical systems. The chemistry time scale can vary widely with temperature and process and is not shown. The thermal diffusivity and diffusivity have been approximated to vary between 0.1 and 1 $cm^2 s^{-1}$ (the latter is more typical under operating conditions). The reactor length is taken to be between 1 and 5 cm, the wall thickness as 300 μm and the gap size to vary between 200 μm and 2 mm.

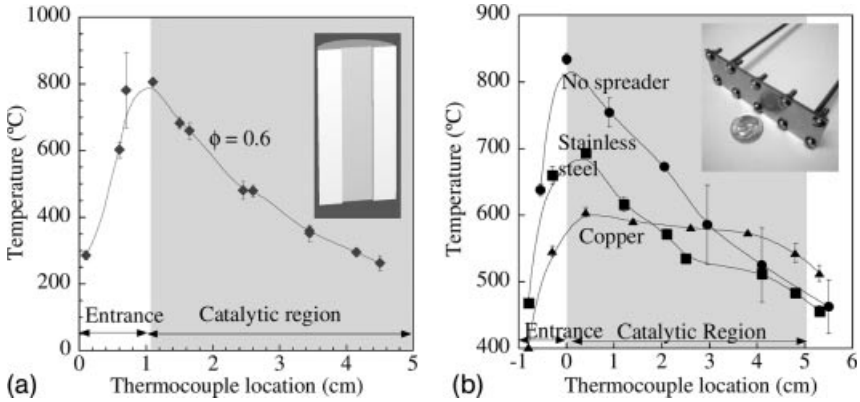

Figure 10.2 Longitudinal temperature profiles at autothermal operation for a H_2–air mixture of equivalence ratio 0.6 in (a) a 250 μm gap size ceramic-frame microreactor and (b) a 300 μm gap size thin stainless-steel-based frame microreactor, for different thermal spreaders (material indicated) of thickness 3.2 mm adhered to the framework (redrawn from [6, 7]). In both cases, Pt/alumina catalyst is used. As the effective wall material conductivity increases, the temperature uniformity improves. In ceramic microburners, the catalyst is brushed on the alumina, whereas in metallic microburners, Pt is impregnated in anodized alumina wafers that are inserted into the structure. The insets show these microreactors.

For highly exothermic or endothermic, fast reactions, where heat is liberated much faster than is dissipated in the axial direction, large axial temperature gradients develop, [6, 7] as shown in Figure 10.2. The isothermicity assumption breaks down for such systems. Likewise, computational fluid dynamics (CFD) simulations for homogeneous combustion (see Figure 10.3 for a representative example) reveal that the axial thermal gradients are even larger for homogeneous combustion due to higher activation energies and volumetric heat release to the lower gas-phase heat capacity. These gradients can be diminished or even eliminated by increasing the effective conductivity (Figure 10.2b) and/or the thickness of the wall.

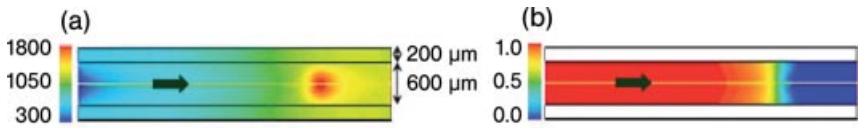

Figure 10.3 Contours of (a) temperature (K) and (b) propane mass fraction from CFD simulations for homogeneous propane–air combustion at equivalence ratio 0.75. These parameters [wall thermal conductivity $k_s = 7.5\ \mathrm{W\,m^{-1}\,K^{-1}}$ and (outside) heat loss coefficient $h_\infty = 25\ \mathrm{W\,m^{-2}\,K^{-1}}$] are close to the extinction limit. Significant gradients exist even in a microburner of 600 μm gap.

10.2.2
Transverse External Thermal Gradients

Since the flow in microchannels is laminar, the boundary layer essentially occupies the entire channel width. The results in Figures 10.3 and 10.10 show that microchemical systems can exhibit substantial gradients – for both homogeneous and catalytic combustion, respectively, – mainly in the longitudinal direction but to some extent also in the transverse direction (between the bulk gas and the surface of the catalyst). Due to the small thickness of the reactor solid structure compared with the reactor length, the inner and outer surfaces of the walls are at the same temperature and the transverse gradients in the walls are negligible (Figure 10.1). Transverse temperature gradients in the gas phase, however, do exist and are especially large near the entrance and at the light-off point.

10.2.3
Transverse External Mass Transfer

The existence of transverse gradients is associated with external mass transfer limitation. The lack of gradients in a CFD simulation is associated with kinetically limited processes. A more quantitative measure of transport or kinetic limitations can be done using an estimate (order of magnitude) of the second Damkhöler number [8]:

$$Da = \frac{\tau_d}{\tau_r} = \frac{d^2/D}{1/k_r} \tag{10.1}$$

where D is the diffusivity.

A decrease in the characteristic dimension of the system (see schematic of parallel plate microreactor in Figure 10.4c) increases the rate of mass transport from the bulk gas to the reactor walls and changes Da. When $Da < 0.1$, surface reaction is limiting and when $Da > 10$, mass transfer is limiting. The pseudo-first-order reaction rate constant is estimated from $k_r = \sigma\ \underline{a}/C$, where σ is the rate of fuel consumption (coming from a detailed model), $\underline{a} = 2/d$ is the catalyst area per unit volume and C is the concentration of the fuel.

Da varies with position due to variation mainly of the reaction time scale as a result of both temperature and concentration gradients. A single location value (e.g. entrance or exit, depending on where the reaction is faster) may be used to provide a conservative estimate of external mass transfer limitations (see an example in Figure 10.4b). An operation diagram can then be constructed for Da versus parallel plate separation (gap size) for different flow rates, temperatures, etc., to indicate mass (or heat) transfer-limited conditions versus kinetically limited conditions (Figure 10.4a). In this example, ammonia decomposition on an Ru catalyst for H_2 production ($2NH_3 \rightarrow N_2 + 3H_2$) and propane combustion on Pt ($C_3H_8 + 5O_2 \rightarrow 3\ CO_2 + 4H_2O$) are studied. The shaded region ($Da < 0.1$) indicates the reaction-limited regime within which the plates are sufficiently close to eliminate mass transfer limitations. For this example, NH_3 operation typically happens in the kinetically

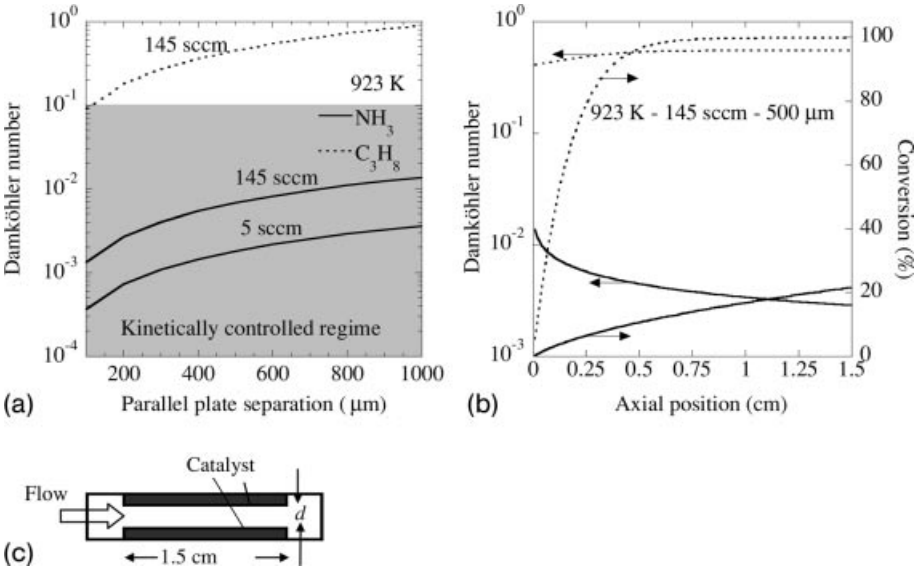

Figure 10.4 (a) *Da* at 1.5 mm from the entrance in an isothermal parallel plate reactor as a function of the parallel plate separation at a temperature and flow rate(s) indicated. (b) *Da* and fuel conversion as a function of the axial position at a temperature and flow rate indicated. (c) Schematic of the reactor geometry. Simulations are shown for both NH_3 cracking on an Ru catalyst for H_2 production and C_3H_8 combustion in air on a Pt catalyst for heat generation.

limited regime, whereas propane, whose chemistry is faster, is in the transition regime despite the plates being sufficiently close. As temperature increases, the reaction rate increases and, thus, operation may change from the kinetically to the transport-controlled regime. At higher temperatures, detailed determination of transverse transport rates is then important for accuracy of model predictions. The same conclusion applies when intrinsic kinetics need to be extracted at high temperatures.

As the channel width shrinks, transverse rates of transport increase at the expense of enhanced pressure drop. Consequently, one should make microreactors small, but not too small. An operation diagram, similar to that one shown in Figure 10.4a, can provide the necessary size for operating in the kinetically limiting regime. These simple analysis results can be verified via detailed CFD simulations [2]. This dimensional group concept can also be used for complex geometries [2], such as the post-microreactor [9, 10], to estimate the distance of structural elements in order to ensure kinetic control.

10.2.4
Internal Heat and Mass Transfer

Due to sheer size of microreactors, catalyst pellets or other structural elements have to be in the micrometer regime. However, packing of a few pellets in a narrow

channel can create a bypass between the reactor bed and the walls and result in a large pressure drop. Instead, it is fairly common to deposit a thin layer of catalyst on the walls. The smaller size of these catalyst systems, compared with many conventional ones, reduces the possibility of internal mass transfer. This fact in turn increases the effective rate of the process and results in process intensification. Conventional analysis of internal heat and mass transfer can be employed to assess the importance of internal transport limitations.

10.3
Thermal Radiation in Microchannels

Autonomous microreactors used for power generation applications utilize energy released from combustion to drive endothermic, hydrogen generation reactions for PEM fuel cells. Often, the wall temperatures in these devices exceed 1200 K [4]. Likewise, the short contact-time reactors rely on high temperatures to ensure complete conversion [11]. Since thermal radiation scales with the fourth power of temperature, it is expected to play a significant role at the operating temperatures of these microreactors. Still, it is common to neglect radiation for reasons explained in this section.

Although the reacting mixture contains various polyatomic gases, the optical length for radiation is very small owing to the narrow channel widths. The optical thickness is measured by the product of absorption coefficient (k_a) and a characteristic dimension of the system, d, that represents an average beam length in the domain. Typical values of k_a in combustion chambers are between 0 and 5 m^{-1}. Furthermore, as already mentioned, a typical diameter or gap size of the microreactors examined in this chapter is on the order of hundreds of micrometers. Therefore, $k_a d \ll 1$ and therefore the medium can be considered as non-participating for radiative heat transfer. The reactor walls are assumed to be diffuse gray emitters and reflectors of radiation. With these assumptions, the net radiosity method can be used to compute the surface-to-surface radiation [12]. A typical radiation flux thus computed in [13] for a microreactor with a channel diameter of 500 μm and a length of 11.6 cm is of the order of $O(10^3)$, whereas the heat of reaction, $O(10^4–10^5)$ W m^{-2} K^{-1}, is substantially higher. The effect of radiation on the wall temperature profile is shown in Figure 10.5. There is only a marginal change in the reactor temperature; the temperature profile shifts upstream by only about two diameters (i.e. ~0.1 cm). Since the aspect ratio, L/d, is very large, the main effect of radiation is to increase the "apparent" wall thermal conductivity. The reason for this is clear from the view factor graphs in Figure 10.6: as the view factor diminishes rapidly with axial distance, most of the radiation emitted by a differential ring element of the microreactor is absorbed by itself and very little energy is transferred to other parts of the reactor.

The dip in the temperature at the reactor end is observed because the wall loses energy by radiation to the surroundings. In this case, a "thermal reservoir" for radiative heat transport at the reactor end was assumed to be at ambient (low) temperature. On the other hand, it is common to use a thermal reservoir temperature

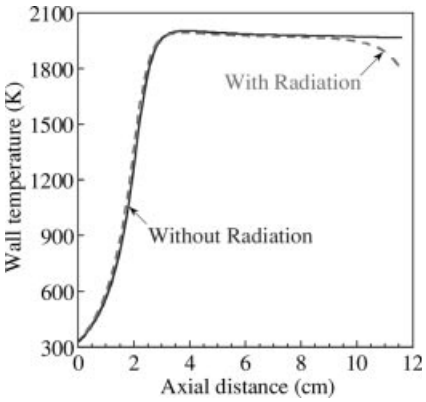

Figure 10.5 Effect of radiation on the temperature profile in a microreactor. The temperature shifts approximately two diameters upstream when radiation is accounted for. Redrawn from [8].

equal to the temperature of exit gases; in this case, a temperature dip is not observed [12, 14].

Boehman [15] made similar observations in his work comparing channels with different aspect ratios and wall emissivities. As the aspect ratio decreases, the effect of radiation increases. For microreactors with smaller aspect ratio, the radiation flux can be computed with reasonable accuracy employing a blackbody assumption for the reactor wall. This assumption reduces the computational complexity in obtaining the radiation flux: the net radiation equation for gray diffuse emitters involves solving an integro-differential equation, which can be avoided with the blackbody radiation flux assumption [15]. Fu *et al.* [16] reported that the radiation effect becomes significant

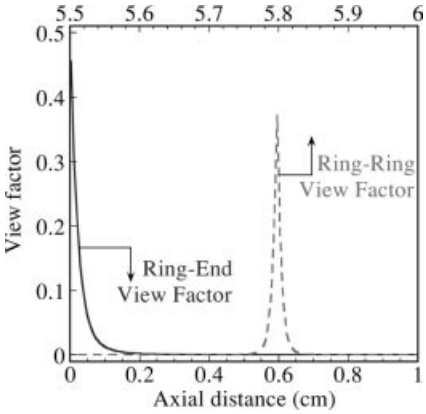

Figure 10.6 The ring–ring view factor (solid line) and ring-end view factor (dashed line) diminish rapidly with axial distance in microchannels of a large aspect ratio, based on simulations in [8].

for circular channels with an aspect ratio of 10; the flame shifts upstream by 1–2 diameters and a slight decrease in the total temperature is observed. The blackbody assumption gives a good estimate of the role of radiation. Karagiannidis *et al.* [14] demonstrated that the radiation effect in catalytic parallel plate reactors of the same aspect ratio (of 10) is even greater: a temperature drop of over 150 °C was observed with an emissivity of 0.6 and the temperature decreased further with the blackbody assumption. The blackbody assumption provided the upper limit for surface-to-surface radiation effects in the microreactor.

An alternative to the above modeling approach is to simulate thermal radiation exchange using a conservative variant of the discrete ordinates (DO) radiation model, called the finite-volume (FV) scheme, implemented in the Fluent software package. The DO–FV model [17] solves the radiative transfer equation (RTE) as a field equation for a finite number of discrete solid angles each associated with a vector direction $\boldsymbol{s}$ fixed in the global Cartesian system. The procedure involves the solution of as many transport equations as there are solid angles.

Propane gas combustion in a microreactor with a channel gap of 1 mm and a length of 6 cm is simulated in 2D using CFD. In these calculations, the angular space is discretized into 64 ($=4N_\Theta N_\Phi$) solid (control) angles that are defined by four polar divisions (N_Θ) and four azimuthal divisions (N_Φ). Opaque, gray diffuse surfaces are assumed. The index of refraction and surface emissivity are set to 1 and scattering is neglected. Unlike the surface-to-surface model, the DO–FV method accounts for gas-to-gas and gas-to-surface radiation and works across the range of optical thicknesses. Finally, the weighted sum of gray gases method [18] is used to calculate the gas absorption coefficient in each control volume. This is a reasonable compromise between the oversimplified gray gas model and banded gas models that take into account absorption in individual absorption bands. Figure 10.7b indicates a small

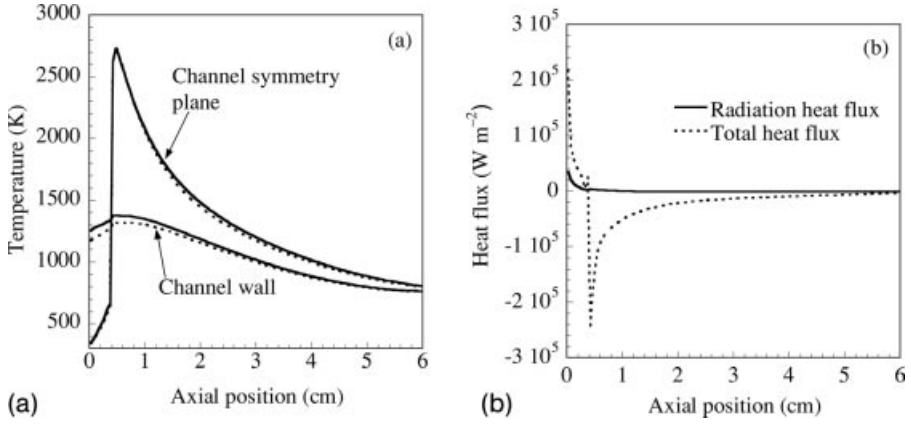

Figure 10.7 (a) Symmetry and channel wall temperature profiles along the reactor length. Solid lines, without radiation; dashed lines, with radiation. (b) Heat flux profile along the upper channel wall when accounting for radiation. Heat flux into the channel is positive; heat flux out of the channel is negative.

contribution of radiation to the total heat flux very near the entrance, where there is a large temperature difference between the hot wall and the cold reactants. This small radiative heat flux contribution is also reflected in the wall temperature profiles very near the entrance, as shown in Figure 10.7a.

In conclusion, radiation effects can be neglected for large aspect ratios typical of microreactors. Blackbody radiation may be used to approximate radiation effects with reduced computational complexity of surface-to-surface radiation. However, for an aspect ratio of 10 or lower, blackbody radiation gives the upper limit of the radiation effect and the net radiation equation needs to be solved to obtain the radiation heat transfer. Heat transfer along the wall is the most critical heat transfer mechanism and needs to be accounted for.

10.4 Transverse Heat and Mass Transfer Correlations

Despite the small gap size, transverse temperature and concentration gradients may exist in microchannels. These gradients depend on the rates of heat and mass transfer versus the rate of reaction. *Da*, as discussed above, provides an estimate of transport effects but cannot be used for quantitative modeling. The Nusselt number (*Nu*) and Sherwood number (*Sh*) provide the heat and mass transfer coefficients, respectively, between a surface and the bulk gas, in the direction perpendicular to the flow. They are defined as ratios of heat or mass flux at the boundary to the net flux between the bulk and the surface:

$$Nu = \frac{dh_g}{k_{cm}} = \frac{d\left(k\frac{dT_g}{dy}\right)_{wall}}{k_{cm}(T_s - T_{cm})} \tag{10.2}$$

$$Sh_k = \frac{dk_{mt,k}}{D_{k,cm}} = \frac{d\left(D_k\frac{dY_k}{dy}\right)_{wall}}{D_{k,cm}\left(Y_{ks} - Y_{k,cm}\right)}. \tag{10.3}$$

where d is the critical channel dimension (diameter or gap width), k is the thermal conductivity, D_k is the diffusivity, T is the temperature, Y_k is the mass fraction and h_g and k_{mt} are the heat and mass transfer coefficients respectively. The subscript s refers to conditions existing near the wall surface and cm refers to the cup-mixing averaged value in the bulk fluid. From these correlations, effective heat and mass transfer coefficients can be obtained:

$$h_g = Nu\frac{k_g}{d} \quad \text{and} \quad k_{mt,k} = Sh\frac{D_{k,cm}}{d}. \tag{10.4}$$

Nu and *Sh* correlations developed for laminar flow [19] are often used to obtain transverse transport in both micro- and macroscale reactors [20]. Since the older correlations were developed using simplifying assumptions, they are not applicable for highly exothermic reacting flows and new correlations have been developed since [21, 22].

Heat and mass transfer coefficients can be used to interrogate the importance of external transport phenomena and how to choose reactor size. The latter controls (i) pressure drop, (ii) residence time and thus reactant conversion or flow rate and thus power generated, (iii) the effective reaction rate and thus the process efficiency, (iv) the temperature and (v) whether a system is kinetically controlled and thus ideal for extraction of catalytic kinetics. Another application of *Nu* and *Sh* is that a 2D or 3D problem can be reduced to a computationally tractable problem by approximating the transverse transport phenomena using overall transport correlations. Such pseudo-2D models (also called heterogeneous 1D models for catalytic systems) have been used to explore the stability and performance of microburners with a significantly lower computational effort than CFD models (e.g. [23–25]).

Pseudo-2D models can be especially valuable when a hierarchical strategy is employed, wherein CFD simulations are employed to obtain the transverse transport correlations that are then used in pseudo-2D models [26]. Results using this strategy for non-adiabatic microburners are presented in subsequent sections. We use Fluent 6.2 [27] to solve a 2D elliptic model for the combined flow, transport and reaction problem. To ensure accuracy of the *Nu* and *Sh* values computed, a non-uniform grid is chosen such that the smallest cell is 1 μm wide in the transverse direction in the fluid phase near the reactor wall. Simulations are performed for various operating conditions and *Nu* and *Sh* are computed using Equations (10.2) and (10.3).

10.5
Homogeneous Microburners

10.5.1
Effect of Transverse Transport on Flame Stability

An example of a CFD simulation depicting a homogeneous, gas-phase microflame stabilized between two parallel plates is shown in Figure 10.3. Figure 10.8 summarizes the effect of transverse heat and mass transfer on flame propagation in a tubular geometry. It depicts the dimensionless temperature (over the ignition temperature) at the reactor inlet versus overall heat transfer coefficient (accounting for wall plus outside heat resistances) for three radii and various radical sticking coefficients, *s*, indicated, for propagation of methane–air flames in a tubular microchannel [1]. For inlet temperatures below each curve, flames do not propagate. Conversely, for inlet temperatures above each curve, flames propagate. The overall heat transfer coefficient captures either heat loss of a standalone microburner or heat exchange with adjacent microreactors carrying out endothermic reaction(s). A flame loses stability either because too much heat is lost via the walls or radicals recombine at the walls and deprive the chemistry from active carriers of combustion.

For large reactors ($R > \sim 10$ mm), a flame propagates through a tube once ignited. There is no visible effect from either instability mechanism. Transverse heat transfer/loss becomes important only at the meso- and microscales ($R < \sim 2$ mm); the stability of the conventional, large-scale burners is unaffected from heat losses/heat

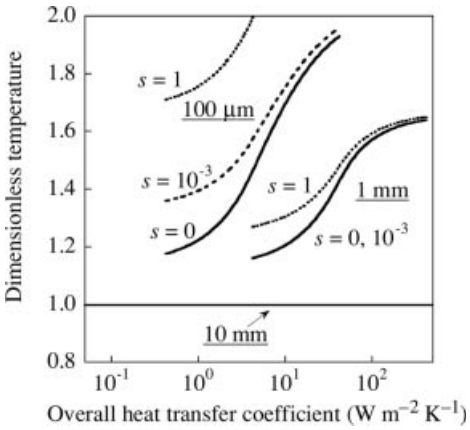

Figure 10.8 Dimensionless temperature (over the ignition temperature) at the reactor inlet versus overall heat transfer coefficient (accounting for wall plus outside heat resistances) for three radii and various radical sticking coefficients, s, indicated, for propagation of methane–air flames in a tubular microchannel (from [1]). For inlet temperatures below each curve, flames do not propagate. Conversely, for inlet temperatures above each curve, flames propagate. The overall heat transfer coefficient captures either heat loss of a standalone burner or heat exchange with adjacent microreactors carrying out endothermic reaction(s). The boundary layer approximation and detailed gas-phase chemistry have been employed for these 2D CFD simulations.

exchange. As the heat loss/heat exchange increases, flame propagation becomes more difficult, i.e. higher preheating (inlet temperatures) is needed to ensure flame propagation, as the upward curves in Figure 10.8 indicate.

All materials exhibit some affinity for adsorption of radicals that are needed for driving the chemistry. Metals adsorb radicals more easily (a large sticking coefficient, s) than ceramics (low s). The importance of radical mass transfer from the bulk of the fluid towards the wall depends on materials and reactor size. For wide tubes (e.g. a radius $R = 10$ mm), flame propagation is robust, i.e. neither radical quenching nor thermal quenching plays any role, as shown in Figure 10.8. For mesoscale radius tubes (e.g. $R = 1$ mm), low sticking coefficients ($s \leq 10^{-3}$) give practically the same results as non-adsorbing walls ($s = 0$). Only high sticking coefficients ($s \approx 1$) moderately affect flame propagation. In contrast, flame quenching (via transverse heat loss) is important. Radical quenching at the walls becomes the dominant stability mechanism only for microscale burners ($R < 1$ mm).

The importance of transverse transport phenomena in homogeneous microburners can be rationalized using the Da analysis introduced in Equation (10.1). For combustion reactions, the reaction time scale τ_r is of the order of 1 ms. Accounting for the temperature effect on diffusivity, the time scale of diffusion τ_d varies from $\sim$1 s to 0.1 ms as the radius R decreases from 1 cm to 100 μm (see Figure 10.1 for the typical range of time scales of microsystems). The radius at which the time scales of transverse mass transfer and chemistry become comparable ($Da = 1$) is estimated to be 300 μm. This approximate estimate is in good agreement with the results shown in

Figure 10.8. This simple dimensionless group analysis clearly indicates that radical quenching at walls is a rather unique attribute of microscales.

Despite belief to the contrary, experiments indicate that self-sustained gas-phase combustion is possible in microburners with gaps smaller than 1 mm [28, 29]. Based on the results in Figure 10.8, this can be achieved by making walls as radical quenchless as possible (via appropriate choice of materials and defect elimination by suitable annealing to avoid radical adsorption) and via suitable thermal management (insulation, heat recirculation, etc.).

10.5.2
Transverse Heat Transfer and Nusselt Number

Norton and Vlachos [30] analyzed the variation in the *Nu* profile along the axial length of a parallel plate microburner. Figure 10.9 shows the *Nu* profile for a stoichiometric propane–air mixture. *Nu* displays a non-monotonic behavior, with a decrease near the entrance and a jump or a discontinuity at the light-off point. Such a discontinuity is often termed a "new entrance effect" because it qualitatively mimics the entrance effect, i.e. an exponential decrease until *Nu* reaches an asymptotic limit followed by a jump. These results are similar to those reported in [31] with a thin-wall approximation. The thin-wall approximation is unsuitable in a microburner because the walls play a major role via axial heat recirculation and affect the gas-phase transport due to the close gas–solid coupling.

A gas-phase microburner can be axially divided into three zones: preheating zone, combustion zone and post-combustion zone. Given that radiative heat transfer is not as important and gas-phase conductivity is low, the burner walls are primarily responsible for heat recirculation, which is essential for heating up the inlet gases, via wall conduction, to their ignition temperature in the preheating zone. Thus, heat

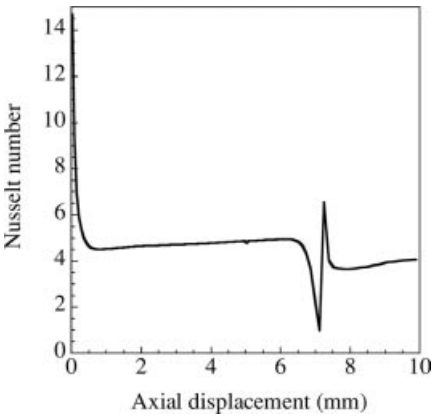

Figure 10.9 Variation of the Nusselt number with axial displacement in a homogeneous microburner of 600 μm gap, 1 cm length, an inlet velocity of 0.83 m s^{-1} and a wall thermal conductivity of 1 W m^{-1} K^{-1} (redrawn from [30]).

transfer takes place from hot walls to cold gases in this zone. At the light-off point, the gas temperature increases due to heat released from the combustion and is accompanied by a large increase in the bulk gas temperature. In the combustion and post-combustion zones, heat transfer predominantly takes place from the hot gases to the burner walls. This dual heat source/heat sink nature of the wall manifests itself as a discontinuity in the *Nu* profile and is located at the light-off point. The substantial role of heat transfer via the walls is a rather unique attribute of microscale exothermic reacting flows.

10.6
Catalytic Microreactors

Figure 10.10a shows propane conversion contours obtained from 2D CFD calculations for catalytic propane combustion in a non-adiabatic microchannel for the conditions mentioned in the caption [23]. Unlike the homogeneous combustion case, the preheating and combustion zones in catalytic microburners overlap since catalytic reactions can occur on the hot catalyst surface close to the reactor entrance. Figure 10.10b shows a discontinuity in the *Nu* profile, similar to the homogeneous combustion problem. In this case, it happens at the boundary between the preheating/combustion zone and the post-combustion zone. At this point, the bulk gas temperature (cup-mixing average) and wall temperatures cross over and the direction

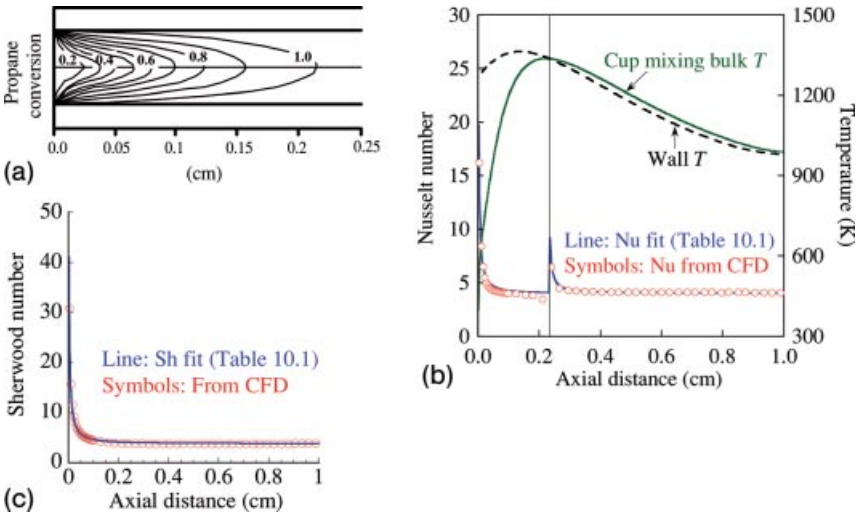

Figure 10.10 (a) Contours of propane conversion computed from CFD simulations in propane–air combustion on Pt. Parameters: wall conductivity $k_s = 2\,\mathrm{W\,m^{-1}\,K^{-1}}$, outside heat loss coefficient $h_\infty = 20\,\mathrm{W\,m^{-2}\,K^{-1}}$, equivalence ratio $\phi = 0.75$ and an inlet velocity $u_0 = 0.5\,\mathrm{m\,s^{-1}}$. (b) Axial profiles of the Nusselt number (symbols) and averaged gas and surface temperatures, and the Nusselt number fit (line) calculated from Table 10.1. A jump in the *Nu* profile occurs when the gas and wall temperatures cross (indicated with a thin vertical line). Redrawn from [23].

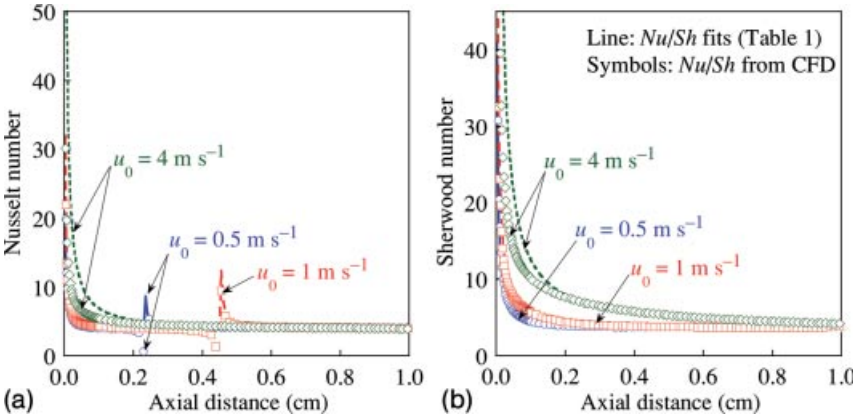

Figure 10.11 Variation in Nusselt and Sherwood number profiles with inlet flow velocity, u_0; other conditions are the same as those in Figure 10.10. The inlet *Pe* varies from 14 to 115 in the curves shown in this figure.

of heat transfer changes sign. In their study of adiabatic microburners, Di Benedetto *et al.* [32] did not observe a discontinuity in *Nu* profile; in the absence of a heat loss mechanism, there is no change in the direction of heat transfer in the post-combustion zone. In contrast to *Nu*, *Sh* varies monotonically, as shown in Figure 10.10c, and settles asymptotically at a value equivalent to the constant temperature asymptote of the analogous Graetz problem.

The inlet velocity significantly modifies the Nu and Sh number profiles near the entrance, as shown in Figure 10.11. As the velocity increases, a larger axial distance is required for the thermal boundary layer to develop fully. Hence *Nu* and *Sh* approach their asymptotic values more gradually. In contrast, other parameters, such as the wall conductivity (k_s), heat loss coefficient (h_∞) to the environment and equivalence ratio (ϕ), do not have an effect on the *Sh* profile. While the *Nu* profile is also independent of these parameters, the location of the discontinuity in the *Nu* profile shifts due to a shift in the boundary between preheating/combustion and post-combustion zones.

Given the profiles depicted in Figure 10.10 and Figure 10.11, one would like to develop suitable correlations. Donsi *et al.* [33] studied the effect of varying *Pe* on the *Nu* profiles for the Graetz problem and used the following general expressions

$$Nu = Nu_\infty \left(1 + \frac{b}{X^*}\right)^\beta$$
$$X^* = \frac{x}{d\ Re\ Pr} \tag{10.5}$$

where Nu_∞ is the asymptotic Nusselt number, X^* is the dimensionless axial distance and *Re* and *Pr* are the Reynolds and Prandtl numbers, respectively. In general, *b* and β can be functions of *Pe*. These expressions are a good starting point for exploring correlations in microchemical systems.

In the preheating zone of microburners, CFD indicates that the asymptotic Nu_∞ value tends towards the constant temperature condition of the Graetz problem

(i.e. 3.8), whereas in the post-reaction zone, the asymptotic value is equal to the constant heat flux value of 4.15. The boundary between the two zones is demarcated with a crossover between the wall and the average gas temperatures. The *Sh* profile is smoother than that of *Nu*; its asymptotic value is 3.8, which is equal to the constant temperature asymptote for the equivalent heat transfer problem. Instead of using Equation (10.5), the following modified form is used:

$$Nu; \quad Sh = A_0\left(1 + \frac{b}{X^*}\right)^{\beta} \qquad X^*_{Nu} = \frac{x}{d\ Re\ Pr},\ X^*_{Sh} = \frac{x}{d\ Re\ Sc} \tag{10.6}$$

where x is the axial distance, d is the gap width and A_0, b and β are parameters fitted to the *Nu* and *Sh* data. Due to the non-monotonic nature of the *Nu* profiles, A_0 is not necessarily the asymptotic value Nu_∞. The parameters for *Nu* and *Sh* fits are given in Table 10.1. The comparison between the computed values (from CFD) and the fits are shown in Figures 10.10 and 10.11. In most cases, the fits are good, but they deteriorate somewhat for faster flows.

Alternatively, the dimensionless groups can be set constant in the pseudo-2D model using a crude average of the asymptotes of the two zones in the case of *Nu*. The last row in Table 10.1 shows such constant (i.e. not a function of axial distance) *Nu* and *Sh* (round) values.

To assess the validity of these correlations, simulations were performed in three different ways: (a) 2D CFD simulations using Fluent, (b) pseudo-2D simulations employing *Nu* and *Sh* correlations according to Equation (10.6) and (c) pseudo-2D simulations employing the constant *Nu* and *Sh* values. The parameters for the last two cases are given in Table 10.1. Simulations were performed for a wide range of parameters of interest; results from one such representative case are shown in Figure 10.12. The symbols represent results from CFD simulations, with the bulk gas quantities reported as cup-mixing average values. The solid and dashed lines represent axially varying and constant *Nu* and *Sh* values, respectively. The conditions in Figure 10.12 were close to extinction, i.e. far away from the conditions under which

Table 10.1 Parameters for computing the Nusselt number (*Nu*) and Sherwood number (*Sh*) in the pseudo-2D model. The two columns of *Nu* values indicate the asymptotic values in the preheating zone (pre) and post-reaction zone (post). The last row indicates constant values used (these are crude averages for *Nu* values between the two zones).

	Nu_{pre}	Nu_{post}	*Sh*
Nu_∞ or Sh_∞	3.8	4.15	3.8
A_0	3.8	4.0	3.72
b	0.025	0.025	0.055
β	0.9	0.9	0.8
Constant	4.0	4.0	3.8

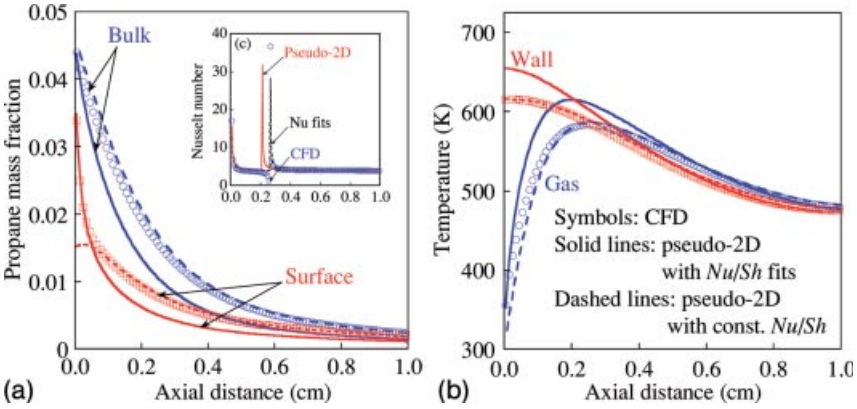

Figure 10.12 Comparison of the axial profiles of (a) propane mass fraction, (b) wall and bulk gas temperature and (c) Nusselt number obtained from CFD simulations (symbols), pseudo-2D model with *Nu*/*Sh* fits (solid lines) and pseudo-2D model with constant *Nu*/*Sh* (dashed lines) near extinction, i.e. with $k_s = 20\,\mathrm{W/m^{-1}\,K^{-1}}$, $u_0 = 0.5\,\mathrm{m\,s^{-1}}$, $\phi = 0.75$ and $h_\infty = 135\,\mathrm{W\,m^{-2}\,K^{-1}}$. The dashed line in (c) shows that the simulation using constant *Nu* and *Sh* values (last row of Table 10.1) closely follows the CFD profile. The solution of the pseudo-2D model using transport correlations is not as accurate since it does not capture the location of the discontinuity in *Nu*.

values in Table 10.1 were developed. The results clearly show that the pseudo-2D model is capable of capturing all the trends of the CFD simulations reasonably (quantitative deviations in temperature and species profiles do exist). Interestingly, for the specific conditions shown in Figure 10.12, the constant *Nu*/*Sh* values capture CFD results more closely than those using the *Nu*/*Sh* correlation fits. A plausible reason for this is that the *Nu* profile computed by solving the balance equations

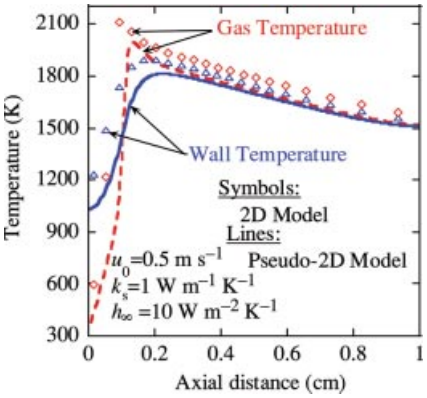

Figure 10.13 Comparison between temperature profiles predicted by the 2D CFD model and pseudo-2D model for homogeneous combustion of a stoichiometric propane–air mixture using a constant *Nu* value (last row of Table 10.1). Redrawn from [18].

simultaneously (solid line) does not accurately predict the location of the discontinuity in the *Nu* values. The model fit becomes better if the *Nu* discontinuity is fixed at the location determined via CFD simulations (dashed line). Similarly to a catalytic microburner, a constant value of $Nu = 4.0$ was able to reproduce the trends of CFD simulations of a homogeneous microburner, as shown in Figure 10.13. Overall, it appears that approximate values (last row of Table 10.1) are sufficient to account for predicting trends and possible semi-quantitative agreement with CFD. At the same time, prediction of the reaction front, where a discontinuity in *Nu* occurs, is a prerequisite for using the above-derived correlations and improve accuracy.

10.7 Conclusions

Despite microscale devices being small, transport phenomena are still potentially important. Simple dimensionless groups can be invaluable in providing a first idea as to the importance of transverse external heat and mass transfer rates. Detailed transport correlations in microchemical systems become complex due to the strong thermal coupling of the gas with the wall. Pseudo-2D simulations, with approximate transport coefficients, can reasonably capture detailed CFD simulations, but the latter are still needed for detailed design. Longitudinal temperature profiles are dictated from the heat release or removal rate and the heat conduction time along the wall. For fast chemistries, which are strongly exothermic or endothermic, temperature gradients may be large. These could be eliminated or reduced via suitable thermal management (e.g. by varying the wall conductivity and/or wall thickness). Important differences between microscale and large-scale devices exist. Radical quenching becomes important only at the microscale, due to fast radial mass transfer, and is insignificant for their large-scale counterparts. This observation has important ramifications for the sustainability of gas-phase driven chemistries. An important aspect of reacting flows is their preheating zone. The thermal conductivity of the walls is generally much greater than that of the fluid and the fluid volume of microdevices is fairly small. Since radiation is insignificant in many microdevices, this disparity in conductivities results in the majority of heat being transferred upstream for preheating mainly through the device walls. This is another major conceptual difference from most large-scale devices.

Acknowledgments

This work was funded through the Army Research Laboratory Composite Materials Research program at the University of Delaware Center for Composite Materials, the Army Research Office under contract DAAD19-01-0582 and the National Science Foundation CBET-0729714 program. Any findings, opinions and conclusions or recommendations expressed here are those of the authors and do not necessarily reflect the views of the Army Research Laboratory or the Army Research Office.

References

1 S. Raimondeau, D. G. Norton, D. G. Vlachos, R. I. Masel, Modeling of high temperature microburners, *Proc. Combust. Inst.*, **2003**, *29*, 901–907.

2 D. G. Norton, S. R. Deshmukh, E. D. Wetzel, D. G. Vlachos, Downsizing chemical processes for portable hydrogen production, in *Microreactor Technology and Process Intensification*, ed. Y. Wang, J. D. Holladay, American Chemical Society, New York, **2005**, Vol. *914*, pp. 179–193.

3 S. R. Deshmukh, D. G. Vlachos, CFD simulations of coupled, counter-current combustor/reformer microdevices for hydrogen production, *Ind. Eng. Chem. Res.*, **2005**, *44*, 4982–4992.

4 S. R. Deshmukh, D. G. Vlachos, Effect of flow configuration on the operation of coupled combustor/reformer microdevices for hydrogen production, *Chem. Eng. Sci.*, **2005**, *60*, 5718–5728.

5 S. R. Deshmukh, D. G. Vlachos, Novel micromixers driven by flow instabilities: application to post-reactors, *AIChE J.*, **2005**, *51*, 3193–3204.

6 D. G. Norton, E. R. Wetzel, D. G. Vlachos, Fabrication of single-channel catalytic microburners: effect of confinement on the oxidation of hydrogen/air mixtures, *Ind. Eng. Chem. Res.*, **2004**, *43*, 4833–4840.

7 D. G. Norton, E. D. Wetzel, D. G. Vlachos, Thermal management in catalytic microreactors, *Ind. Eng. Chem. Res.*, **2006**, *45*, 76–84.

8 *Kirk-Othmer Encyclopedia of Chemical Technology*, ed. J. I. Kroschwitz, John Wiley & Sons, Inc., New York, **1999**.

9 S. R. Deshmukh, A. B. Mhadeshwar, M. I. Lebedeva, D. G. Vlachos, From density functional theory to microchemical device homogenization: model prediction of hydrogen production for portable fuel cells, *Int. J. Mult. Comp. Eng.*, **2004**, *2*, 221–238.

10 S. R. Deshmukh, A. B. Mhadeshwar, D. G. Vlachos, Microreactor modeling for hydrogen production from ammonia decomposition on ruthenium, *Ind. Eng. Chem. Res.*, **2004**, *43*, 2986–2999.

11 D. A. Goetsch, L. D. Schmidt, Microsecond catalytic partial oxidation of alkanes, *Science*, **1996**, *271*, 1560–1562.

12 M. F. Modest, *Radiative Heat Transfer*, McGraw-Hill, New York, **1993**.

13 N. S. Kaisare, J. H. Lee, A. G. Fedorov, Hydrogen generation in a reverse-flow microreactor: 1. Model formulation and scaling, *AIChE J.*, **2005**, *51*, 2254–2264.

14 S. Karagiannidis, J. Mantzaras, G. Jackson, K. Boulouchos, Hetero-/homogeneous combustion and stability maps in methane-fueled catalytic microreactors, *Proc. Combust. Inst.*, **2007**, *31*, 1973–1981.

15 A. Boehman, Radiation heat transfer in catalytic monoliths, *AIChE J.*, **1998**, *44*, 2745–2755.

16 X. Fu, R. Viskanta, J. P. Gore, Combustion and heat transfer interaction in a pore-scale refractory tube burner, *J. Thermophys. Heat Transfer*, **1998**, *12*, 164–171.

17 G. D. Raithby, E. H. Chui, A finite-volume method for predicting radiant heat transfer in enclosures with participating media, *J. Heat Transfer*, **1990**, *112*, 415–423.

18 T. F. Smith, Z. F. Shen, J. N. Friedmann, Evaluation of coefficients for the weighted sum of grey gases model, J. Heat Transfer, **1982**, *104*, 602–608.

19 R. K. Shah, A. L. London, *Laminar Flow Forced Convection in Ducts*, Academic Press, New York, **1978**.

20 M. Maestri, A. Beretta, G. Groppi, E. Tronconi, P. Forzatti, Comparison among structured and packed-bed reactors for the catalytic partial oxidation of CH_4 at short contact times, *Catal. Today*, **2005**, *105*, 709–717.

21 G. Groppi, E. Tronconi, P. Forzatti, Mathematical models of catalytic combustors, *Catal. Rev. Sci. Eng.*, **1999**, *41*, 227–254.

22 N. Gupta, V. Balakotaiah, Heat and mass transfer coefficients in catalytic monoliths, *Chem. Eng. Sci.*, **2001**, *56*, 4771–4786.

23 N. S. Kaisare, S. R. Deshmukh, D. G. Vlachos, Stability and Performance of catalytic microreactors: propane catalytic combustion on Pt, *Chem. Eng. Sci.*, **2008**, *63*, 1098–1116.

24 N. S. Kaisare, D. G. Vlachos, Extending the region of stable homogeneous micro-combustion through forced unsteady operation, *Proc. Combust. Inst.*, **2007**, *31*, 3293–3300.

25 N. S. Kaisare, D. G. Vlachos, Optimal reactor dimensions for homogeneous combustion in small channels, *Catal. Today*, **2007**, *120*, 96–106.

26 S. R. Deshmukh, N. S. Kaisare, D. G. Vlachos, Hierarchical modeling of integrated microdevices for hydrogen production, in *IMRET: 9th International Conference on Microreactor Technology*, Potsdam, **2006**.

27 *Fluent 6.2*, Fluent, Lebanon, NH, **2004**.

28 C. M. Miesse, R. I. Masel, C. D. Jensen, M. A. Shannon, M. Short, Submillimeter-scale combustion, *AIChE J.*, **2004**, *50*, 3206–3214.

29 R. I. Masel, M. Shannon, Microcombustor having submillimeter critical dimensions, The Board of Trustees of the University of Illinois, Urbana, IL, US Patent 6193501, 27 February **2001**.

30 D. G. Norton, D. G. Vlachos, A CFD study for propane/air microflame stability, *Combust. Flame*, **2004**, *138*, 97–107.

31 R. H. Heck, J. Wei, J. R. Katzer, Mathematical modeling of monolithic catalysts, *AIChE J.*, **1976**, *22*, 477–484.

32 A. Di Benedetto, F. S. Marra, F. Donsi, G. Russo, Transport phenomena in a catalytic monolith: effect of the superficial reaction, *AIChE J.*, **2006**, *52*, 911–923.

33 F. Donsi, A. Di Benedetto, F. S. Marra, G. Russo, CFD simulation of heat transfer in a circular channel: effect of the Pe number, *Int. J. Chem. Reactor Eng.*, **2005**, *3*, A36, 1–20.